Computational fluid dynamic analysis of an adsorption-based cogeneration osmotic heat engines with stepwise porosity distribution

Yanan Zhao, Mingliang Li, Rui Long [*], Zhichun Liu, Wei Liu

School of Energy and Power Engineering, Huazhong University of Science and Technology, Wuhan 430074, PR China

ABSTRACT

Adsorption-based osmotic heat engines offer an alternative way for converting ultra-low temperature waste heat into electricity. Here, considering the heat and mass transfer characteristics in the adsorbent bed, a computational fluid dynamic model is developed to describe the adsorption-based osmotic heat engine for power and refrigeration cogeneration. Impacts of the porosity distribution, adsorption time, switching time, fin number and working solution-adsorbent pairs on system performance are comprehensively analyzed under different porosity distribution configurations. Results reveal that Configuration I leads to higher coefficient of performance (COP), exergy efficiency. However, Configuration II renders higher electrical efficiency. Compared with the uniform porosity configuration, COP and exergy efficiency are respectively elevated by 1.96% and 1.19% under the stepwise porosity configuration of 0.3–0.5. The electrical efficiency is increased by 15.5% with porosity configuration of 0.7–0.2. LiCl and AQSOA-Z02 under the stepwise porosity configuration of 0.7–0.2 can lead to the highest exergy efficiency of 7.76%.

1. Introduction

Excessive consumption of fossil fuels has resulted in severe climate problems. It is estimated that around 40 % of total greenhouse gases are released from coal-based power plants, which is the main contributor to global warming (Zhao et al., 2021). Many efforts have been devoted to energy saving and emission reduction: (1) Improving the energy conversion efficiency of the existing thermodynamic system via waste heat recovery in power industry (Xie et al., 2022; Raninga et al., 2022); aluminium industry (Brough and Jouhara, 2020), steel sector (Egilegor et al., 2020); *etc*; (2) Extracting electricity from renewable energy sources, such as solar power (Yap et al., 2022), biomass energy (Rahman et al., 2022) and geothermal energy (Zhang et al., 2022); (3) Developing novel high-efficiency energy conversion system with low emission. Recently, the exploitation of waste heat harvested from power plant, renewable energy for electricity generation provides a promising way to reduce carbon emission and alleviate global warming. Several technologies have been developed to utilize those low temperature heat (Zhang et al., 2013; Xia et al., 2019). Organic Rankine cycle (ORC) is extensively applied to utilize low temperature waste heat above 80 °C (Oyekale and Emagbetere, 2022). However, high-performance energy conversion technologies for harvesting low-grade heat with temperature below

80 °C are still absent due to unsatisfied energy conversion efficiency under such low temperature level (Xu et al., 2019).

Recently, the osmotic heat engine (OHE) for converting ultra-low temperature waste heat into electricity has attracted increasing attention due to its high theoretical efficiency. In an osmotic heat engine, saline solution is charged into the regeneration unit and divided into high concentration solution and low concentration solution driven by low-grade heat (Brogioli and Yip, 2022; Prajapati et al., 2022; Hua et al., 2022; Zhang et al., 2023). Then the salinity gradient of the two solutions with different concentrations is captured by the power generation unit to produce useful work (Kim et al., 2020; Marino et al., 2015; Wang et al., 2022; Liu et al., 2022). In turn, the mixed solution withdrawn from the power generation unit is recharged into the regeneration unit to restore the initial concentration. Osmotic heat engine also has the advantage of the absence of environmental impacts due to the closed-loop cycle, no moving parts, flexible selection of artificial working salt solution (Zhao et al., 2022; Tamburini et al., 2016). Many studies regarding osmotic heat engines highlight the system configurations, operating conditions as well as selection of working solvent and solute. Long et al. (Long et al., 2017) conducted a performance investigation of a MD-RED hybrid system considering the heat and mass transfer characteristics in the thermal separation and power generation process. The

---

electric efficiency could reach 1.15 % with hot and cold source temperature of 60 and 20 °C for NaCl solution with concentration of 5 mol/kg. Liu et al. (Liu et al., 2022) employed the unconventional LiBr solution as the working fluid in an RED osmotic heat engine and the effects of the condensation and generation temperature, RED cells temperature and charge concentration on the system efficiency were investigated. The results revealed that increasing the condensation temperature, reducing the generation temperature and charge concentration are beneficial for improving system performance. A maximum energy efficiency of 6.05 % can be obtained at the condensation temperature of 35.16 °C and the generate temperature of 70 °C, respectively. Owing to the merits of ultra-low operating temperature and simple control, adsorption desalination (AD) has also been considered as strong candidate for thermal separation unit of OHEs (Olkis et al., 2019; Zhao et al., 2021). Sztekler et al. (Sztekler et al., 2020; Sztekler et al., 2020) numerically and experimentally investigated the performance of AD as a chiller and desalination device, which also implies the feasibility of AD as a thermal separation unit of OHE.

Olkis et al. (Olkis et al., 2018) introduced the utilization of AD in the closed-loop osmotic heat engine. The combinations of working salt and adsorbent material were optimized and screened by establishing a steady-state model. An energy efficiency of 4 % was obtained. Zhao et al. (Zhao et al., 2020) developed a dynamic model of an AD-RED system considering the refrigeration performance in AD unit. An energy efficiency and coefficient of performance (COP) of 0.84 and 0.39 % were achieved. To step further, the screening of the adsorbent-working solution pairs was conducted based on an experimental water adsorption isotherm database to identify the high-performance working pairs for the AD-RED hybrid system (Zhao et al., 2022).

In previous literatures on adsorption-based osmotic heat engines (Zhao et al., 2022; Long et al., 2021; Olkis et al., 2021), the thermal separation process in AD are numerically described by solving lumped energy and mass balance equations, which implies that the temperature and pressure inside the adsorption bed are assumed to be uniform. Actually, the temperature and adsorption uptake are spatially distributed in the adsorption/desorption process and Computational Fluid Dynamics (CFD) is a well-known tool to analyze the heat and mass transfer in the adsorption bed. Many studies devoting to enhancing the heat and mass transfer in AD process has been carried out. Krzywanski et al. (Krzywanski et al., 2022; Krzywanski et al., 2023) applied fluidization technique to improve the design of the bed in the adsorption chiller. The results showed that the heat transfer coefficient has been efficiently improved in the fluidized bed. Kulakowska et al. (Kulakowska et al., 2020) mixed additives of metal and carbon nanotube into the silica gel-based adsorption bed. And the heat transfer process was significantly improved. Li et al. (Li et al., 2022) also carried out a CFD analysis of a metal foam packed adsorbent bed in an adsorption-based desalination and cooling system. And the performances of cooling and water production are both elevated. Grabowska et al. (Grabowska et al., 2021) built a novel coated construction of adsorption beds to improve the thermal conductivity. And an experimental research was conducted with two kinds of epoxy resins and a maximum thermal conductivity of 0.533 W/(m·K) can be obtained. Some studies also indicate that the geometric structure of the heat exchangers and the distribution of the adsorbent can significantly affect the local heat and mass transfer in adsorption bed, thus the desalination and refrigeration performance. Leong et al. (Leong and Liu, 2004) developed a two-dimensional non-equilibrium model to describe the heat and mass transfer in adsorption bed. And the results showed that COP does not change with the variation of adsorbent bed porosity, while the specific cooling power (SCP) reduces with a decrease in bed porosity when the bed porosity varies from 0.25 to 0.38. Demir et al. (Demir et al., 2009) reported that the increase of porosity reduces the thermal conductivity of the bed, heat transfer rate in the bed and the period of the adsorption process. Li et al. (Li et al., 2021) developed a CFD model of an adsorption cooling system with a gradient porosity distribution bed. Cai et al. (Cai et al., 2023) also

discussed the effect of stepwise porosity distribution on the performance of the adsorption refrigeration. The same conclusion can be drawn that inhomogeneous porosity can significantly affect the heat and mass transfer inside the adsorption bed. Although there have been some studies on heat and mass transfer enhancement in adsorption beds, no literature has reported on adsorption-based osmotic heat engines considering the uneven temperature and adsorption capacity within the adsorption bed.

In this study, we present an innovative adsorption-based osmotic heat engine that combines adsorption separation with reverse electrodialysis to efficiently convert low-grade heat into electricity while also providing cooling power. According to research, it is evident that inhomogeneous pore space can significantly affect the heat and mass transfer characteristics within the adsorption bed. Therefore, a two-dimensional computational fluid dynamic model of a finned-tube adsorption bed with stepwise porosity distributions is developed. Impacts of the stepwise porosity distribution, adsorption time, switching time, fin number and working solution-adsorbent pairs on system performance are also comprehensively analyzed. This work may provide guidance for rational design of high-performance adsorption based OHEs.

2. System description and modelling

2.1. System description

As shown in Fig. 1, the OHE for power and refrigeration cogeneration consists an AD subsystem that thermally separats the saline solution into solutions with high and low concentrations and restore the solutions into the original concentration, and a RED subsystem that converts the Gibbs free energy of mixing the two solutions with different concentrations into electricity. The AD unit consists of four major components of evaporator, condenser, adsorption bed and heat exchanger. After the preliminary preparation of degassing the whole vessel and charging the saline into evaporator, the water evaporates from the evaporator and then is adsorbed by highly hydrophilic adsorbent with adsorption bed chamber connecting with the evaporator and isolating from the condenser. Meanwhile, the water evaporated removed the heat from the refrigerant, offering cooling power to the external environment as well as concentrating the residual solution in the evaporator. During the adsorption process, the adsorption heat is removed by the cooling water flowing through the adsorption bed. During the desorption process, the bed chamber is connected to the condenser and the cooling water is replaced by hot water obtained from low-grade heat. And the water vapor is repelled from the adsorption bed and condensed in the condenser to produce diluted water. A period of switching time is required between the adsorption process and desorption process for precooling and preheating the adsorption bed, when the bed chamber is not connected to either the evaporator or the condenser. Finally, the electricity can be extracted from the Gibbs free energy of mixing the diluted solution and concentrated solution generated from AD unit via RED process.

To reveal the heat and mass transfer characteristics in the adsorption bed, a computational fluid dynamic model of the adsorption bed is established instead of the lumped model. In this study, we mainly focused on the effect of stepwise porosity distributions on system performance. As shown in Fig. 2, a finned-tube heat exchanger is adopted to increase heat exchange area, and adsorbent with stepwise porosity distributions is filled between the adjacent fins. The porosity is stepwisely distributed in the large porosity zone (LPZ) and small porosity zone (SPZ). In order to control the variable, several stepwise porosity distributions (i.e. 0.2–0.5, 0.2–0.6, 0.2–0.7, 0.3–0.5, 0.3–0.6 and 0.3–0.7) under an average bed porosity of 0.4 by volume adjustment are constructed. In this study, the particle size of the adsorbent d_p is assumed to be constant at 0.35 mm, and the variability of porosity can be obtained by adjusting the quality of the filled adsorbent. In practical application,
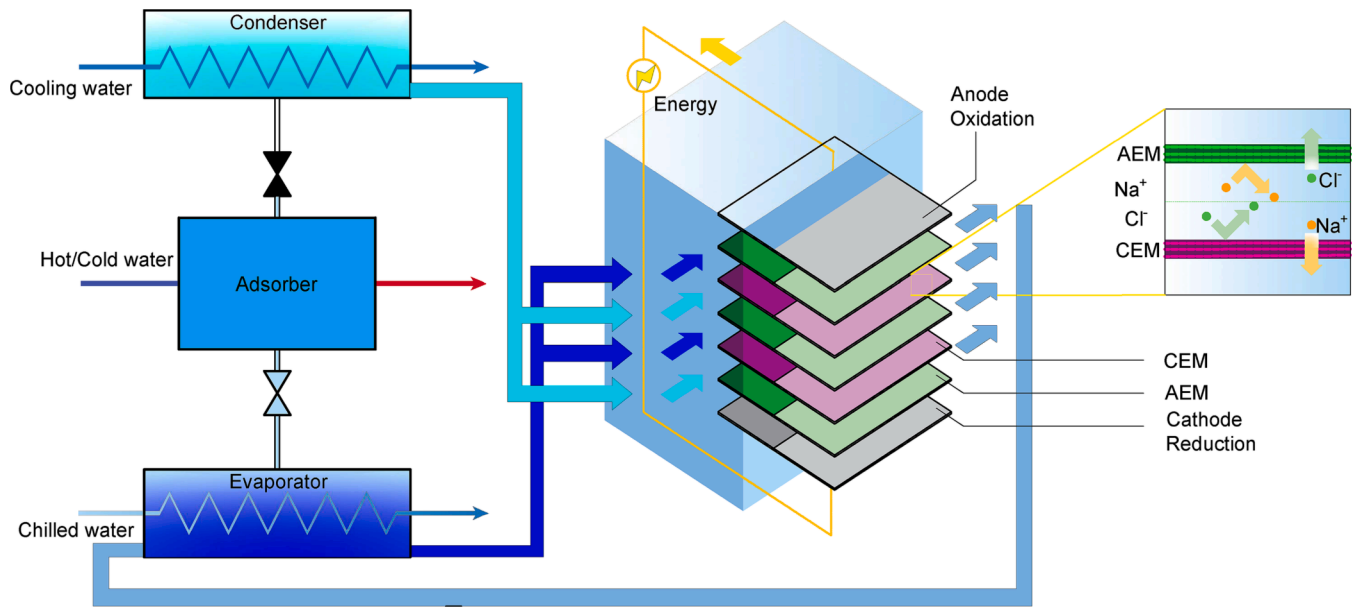
Fig. 1. Schematic diagram of the ohe for cooling and power cogeneration.
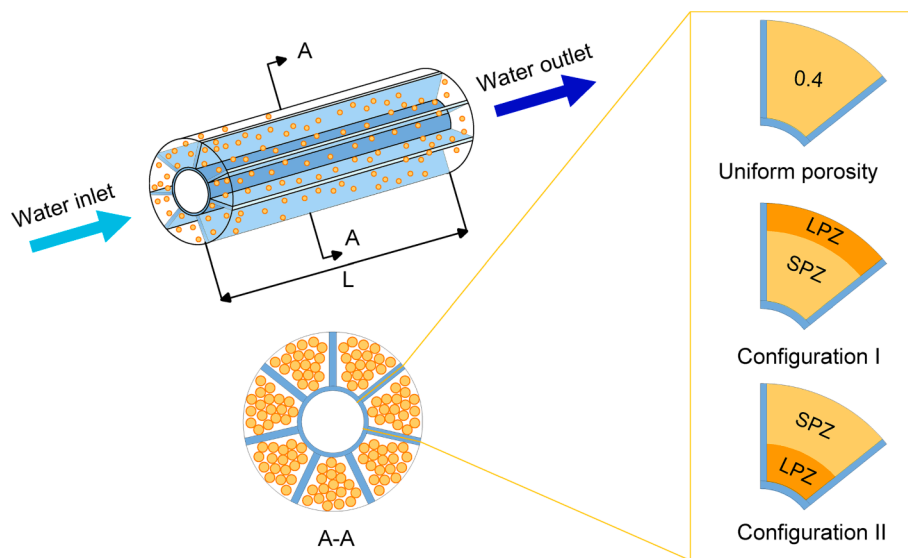

Fig. 2. Schematic diagram of the stepwise porosity distribution of the adsorbent under different configurations.

fixing nets can be used to control the filling quality of the adsorbent, thereby achieving a certain porosity (Cai et al., 2023). Due to the anisotropy of the adsorbent bed, two stepwise porosity distribution exists. In Configuration I, the SPZ is adjacent to the metal heat exchange tube; In Configuration II, the LPZ is adjacent to the metal heat exchange tube. In addition, the performance under a uniform bed porosity of 0.4 has also been investigated for comparison.

2.2. Mathematical modeling

For simplification, the following assumptions have been adopted (Chen and Chua, 2020; Wu et al., 2014): (1) The vapor phase is considered as ideal gas. (2) The temperature and pressure in the evaporator and condenser are assumed to be space-independent and considered as lumped. (3) All the physical properties of the solid materials are constant. (4) There is no adsorption hysteresis.

2.2.1. Adsorbent bed

The mass conservation equation of the adsorbate gas in the adsorption bed is

$$\frac{\partial(\varepsilon_t \rho_\nu)}{\partial t} + \nabla \cdot (\rho_\nu \overrightarrow{U}) + \rho_b \frac{\partial W}{\partial t} = 0 \tag{1}$$

where the three terms on the left side of the equation are the unsteady term, the velocity term and mass source term, respectively. ρ_ν is the density of water vapor. ρ_b is the density of adsorption bed, which equals to the density of the adsorbent (silica gel for default) multiplied by $(1 - \varepsilon_t)$, i.e. $\rho_b = \rho_s(1 - \varepsilon_t)$. ε_t is the total porosity of adsorption bed, which is given by $\varepsilon_t = \varepsilon_b + \varepsilon_p(1 - \varepsilon_b)$, where ε_p and ε_b are the porosity of bed voidage and adsorbent particle. W is the uptake of the adsorbent. During the adsorption process, inertial and viscous terms in the momentum equation are very small due to the low velocity of the adsorbed water vapor flowing through the adsorbent particles, which can be neglected compared with viscous effect. Thus the vapor velocity U can

be obtained by Darcy's Law (Taqvi et al., 1997)

$$\overrightarrow{U} = -\frac{K}{\mu}\nabla P \tag{2}$$

where μ denotes the water vapor viscosity, P is the local pressure and K is the permeability of the adsorption bed, which is given by Blake-Kozeny equation (Bird, 2002)

$$K = \frac{d_p^2 \varepsilon_b^3}{150(1 - \varepsilon_b)^2} \tag{3}$$

where d_p denotes the diameter of the adsorbent particles.

The adsorption kinetics is determined by the linear driving force equation (LDF) to estimate the adsorption/desorption rate as follow

$$\frac{\partial W}{\partial t} = \frac{60 D_{so} e^{-\frac{E_a}{RT_s}}}{d_p^2}(W_0 - W) \tag{4}$$

where D_{so} denotes the pre-exponential kinetic constant, E_a is the diffusion activation energy, R is the universal gas constant, T defines the temperature of the adsorbent, W_0 represents the equilibrium uptake under specific pressure and temperature, which can be obtained by Dubinin-Astakhov equation (Askalany et al., 2012)

$$W_0 = W_\infty \exp\left(-\left(\frac{RT_s}{E}\ln\left(\frac{P_s}{P}\right)\right)^n\right) \tag{5}$$

where W_∞ is the maximum water uptake adsorbed at saturation, E is the characteristic energy, P_s denotes the saturated pressure at the adsorbent temperature of T and n is the heterogeneity factor.

The energy conservation equation in the adsorption bed is (Solmuş et al., 2012)

$$(\varepsilon_b \rho_v C_{pv} + \rho_b C_{ps} + \rho_b W C_{pw})\frac{\partial T_v}{\partial t} + \rho_v C_{pv}\overrightarrow{U}\cdot\nabla T = \nabla\cdot(k_{eff}\nabla T) + \rho_b H_\alpha \frac{\partial W}{\partial t} \tag{6}$$

where C_p is the specific heat capacity, and the subscripts v, s, and w refer to vapor, adsorbent solid and adsorbed water, respectively. k_{eff} is the effective thermal conductivity of the adsorption bed. $k_b = k_v \varepsilon_b + k_s(1 - \varepsilon_b)$, k_v and k_s are the thermal conductivity of the vapor and the adsorbent (silica gel for default), respectively. H_α is the isosteric adsorption heat. The leftmost unsteady-state term on the left side stands for the variations of internal energy over time, the second term on the left side represents the convection term. The first terms on the right side represent conduction term and the second term is the source term which indicates the rate of isosteric heat generation caused by sorption.

The heat conduction in the metal fin tube can be expressed as (Aziz et al., 2012; Mohammed, 2013)

$$\frac{\partial T}{\partial t} = \alpha\nabla^2 T \tag{7}$$

where α denotes the thermal diffusivity of the fin tube.

2.2.2. Evaporator and condenser

The mass balance in the evaporator and condenser is

$$\frac{dM_{s,Evap/cond}}{dt} = -\frac{dW}{dt}M_{sb} \tag{8}$$

where $M_{s,Evap/cond}$ is the solution mass in the evaporator/condenser, and M_{sb} is the mass of the adsorbent.

The energy balance in evaporator and condenser are

$$\left[M_{sw,Evap}c_{p,sw} + M_{HX,Evap}c_{p,HX}\right]\frac{dT_{Evap}}{dt} = -h_{fg}\frac{dW}{dt}M_{sb} + \dot{m}_{ch}c_{p,ch}\left(T_{ch,in} - T_{ch,out}\right) \tag{9}$$

$$\left[M_{w,Cond}c_{p,w} + M_{HX,Cond}c_{p,HX}\right]\frac{dT_{Cond}}{dt} = -h_{fg}\frac{dW}{dt}M_{sb} + \dot{m}_{cw}c_{p,cw}\left(T_{cw,in} - T_{cw,out}\right) \tag{10}$$

where M_{sw} and M_{sw} denotes the saline and water mass in the evaporator and condenser, respectively, M_{HX} is the mass of heat exchanger, h_{fg} is the latent heat of vaporization, the last term on the right side of the equation (9) and equation (10) represents the heat adsorbed from the refrigerant in the evaporator and the heat taken away by the cooling water in the condenser, respectively. The outlet temperature of the fluid flowing through each heat exchanger can be obtained by

$$T_{out} = T_0 + (T_{in} - T_0)\exp\left(\frac{-UA_{HX}}{\dot{m}c_p(T_0)}\right) \tag{11}$$

where T_0 is the temperature of the heat exchanger, $(UA)_{HX}$ is the overall heat transfer coefficient of the heat exchanger.

2.2.3. Initial and boundary conditions

In the evaporator, the saturated pressure is impacted by the dissolvent salt, which can be calculated as (Olkis et al., 2018)

$$p_{eva} = p_{sat}\exp(-\nu C M_w \Phi) \tag{12}$$

where ν and C are the dissociated ions number and molarity, respectively. M_w is the mole mass of the solvent, $P_{sat} = 8.143 \times 10^{10}\exp(-5071.7/T)$ is the saturated pressure of the pure solution under temperature of T. Φ is the osmotic coefficient of the working salt, which can be given by (Pitzer and Mayorga, 1973)

$$\Phi - 1 = |Z_+ Z_-|f^\phi + m[(2\nu_+\nu_-)/\nu]B^\phi + m^2\left[(2\nu_+\nu_-)^{3/2}/\nu\right]C^\phi \tag{13}$$

where Z is the ion charge, m is the molality. The coefficients of f^ϕ, B^ϕ, C^ϕ are calculated as (Pitzer and Mayorga, 1973; Silvester and Pitzer, 1977)

$$f^\phi = -A_\phi I^{1/2}/(1 + bI^{1/2}) \tag{14}$$

$$B^\phi = \beta^{(0)} + \beta^{(1)}\exp(-\alpha_1 I^{1/2}) \tag{15}$$

$$A_\phi = (1/3)(2\pi N\rho)^{1/2}\left(e^2/4\pi\varepsilon_0\varepsilon kT\right)^{3/2} \tag{16}$$

Relevant osmotic coefficients can be found in our previous work (Zhao et al., 2020) and the Pitzer parameters for calculating the osmotic coefficient in this study are listed in Table 1.

In the calculation, temperatures of hot water and cooling water flowing through the finned-tube heat exchanger are set at 85 °C and 30 °C and the convective heat transfer coefficient is set at 500 W/m²·K. The inlet temperatures of the refrigerant and cold water in the evaporator and condenser are both set at 20 °C. The initial temperature of the physical bed is set at 60 °C. The temperature of the evaporator and the condenser are set at 10 °C and 20 °C, respectively. The initial presser in the physical bed is set at the saturated pressure under the evaporation temperature. In the isobaric heating process and desorption process, the temperature of the external hot water is fixed at 85 °C. In the isobaric cooling process and adsorption process, the temperature of the external cold water is fixed at 30 °C. The initial and boundary conditions are

Table 1
Pitzer parameters for salt solutions studied in this work.

Salt	$\beta^{(0)}$	$\beta^{(1)}$	C^ϕ	Ref
NaCl	0.0765	0.2664	0.00127	(Pitzer and Mayorga, 1973)
NaNO₃	0.0068	0.1783	−0.00072	(Pitzer and Mayorga, 1973)
LiCl	0.1494	0.3047	0.00359	(Pitzer and Mayorga, 1973) {Pitzer, 1973 #73}
LiNO₃	0.1420	0.2780	−0.00551	(Pitzer and Mayorga, 1973)
AgNO₃	−0.0856	0.0025	0.00591	(Pitzer and Mayorga, 1973)

further summarized in Table 2 for readability.

2.2.4. Reverse electrodialysis

The Gibbs free energy of mixing the water production in the condenser and the concentrated solution remaining in the evaporator is adopted for estimating the maximum electricity extracted from RED unit. The mole Gibbs free energy of mixing can be calculated as (Yip and Elimelech, 2012)

$$-\Delta G_{mix} = RT \left\{ \left[\sum x_i \ln(\gamma_i x_i) \right]_M - \Lambda_A \left[\sum x_i \ln(\gamma_i x_i) \right]_A - \Lambda_B \left[\sum x_i \ln(\gamma_i x_i) \right]_B \right\} \tag{17}$$

where x_i denotes the mole fraction of species i, the subscripts A, B and M denotes the two solutions with different concentration and the mixture solution, represents the ratio of the moles in the specific solution to the total moles in the final mixture. *is* the activity coefficient for interpreting the behavior of nonideal solutions, which can be calculated by the Pitzer correlations as (Pitzer and Mayorga, 1973)

$$\ln(\gamma) = |z_M z_X| f^\gamma + m \left(\frac{2\nu_X \nu_M}{\nu} \right) B_{MX}^\gamma + m^2 \left(\frac{2(\nu_X \nu_M)^{3/2}}{\nu} \right) C_{MX}^\gamma \tag{18}$$

$$f^\gamma = -A_\phi \left[\frac{I^{1/2}}{1 + bI^{1/2}} + \frac{2}{b} \ln(1 + bI^{1/2}) \right] \tag{19}$$

$$B_{MX}^\gamma = 2\beta_{MX}^{(0)} + \frac{2\beta_{MX}^{(0)}}{\alpha^2 I} [1 - e^{-\alpha I^{1/2}} (1 + \alpha I^{1/2} - (1/2)\alpha^2 I)] \tag{20}$$

$$C_{MX}^\gamma = \frac{2}{3} C_{MX}^\phi \tag{21}$$

For relatively low salt concentration, the effect of salt on the total volume during mixing process is negligible. The Gibbs free energy of mixing can be simplified as (Yip and Elimelech, 2012)

$$-\frac{\Delta G_{mix}}{\nu RT} \approx c_M \ln(\gamma_{s,M} c_M) - \Psi c_{low} \ln(\gamma_{s,low} c_{low}) - (1 - \Psi) c_{high} \ln(\gamma_{s,high} c_{high}) \tag{22}$$

where ν is the total ions number dissociated in the solution and $\Psi \approx V_{low}/(V_{low} + V_{high})$.

2.3. Performance indicators of the cogeneration system

The regeneration heat Q_{reg} indicating the total heat consumption during reheating and desorption process can be obtained by integrating the heat flux at the boundary between the hot water and the finned-tube over time. The estimated maximum electricity extracted from the system can be captured by the Gibbs free energy of mixing ΔG_{mix}. Consequently, the electrical efficiency and electrical power can be calculated as $\eta_e = \frac{\Delta G_{mix}}{Q_{reg}}$ and $P_e = \frac{\Delta G_{mix}}{t_{cycle}}$, respectively. The cooling capacity generated from the evaporator can be obtained by $Q_c = \int_0^{t_{cycle}} \dot{m}_{ch} c_{p,ch} (T_{ch,in} - T_{ch,out}) dt$. Thus, the coefficient of performance and cooling power are given by $COP = Q_c/Q_{des}$ and $P_c = \frac{Q_c}{t_{cycle}}$, respectively. In addition, the exergy efficiency is adopted to estimate the overall performance of the cogenera-

tion system, which can be calculated as $\eta_{ex} = \frac{Q_c \left(\frac{T_{eva}}{T_{ev}} - 1 \right) + \Delta G_{mix}}{Q_{reg} \left(1 - \frac{T_{ev}}{T_{des}} \right)}$, where T_{ev}, T_{eva} and T_{des} are the temperature of the environmental, evaporation temperature and desorption temperature, respectively.

2.4. Grid independence and model validation

The computational fluid dynamic model of the AD unit established by combining a two-dimensional adsorption bed with lumped evaporator/condenser is employed to simulate the thermal separation process of the saline solution via the adsorption bed with finned tube heat exchangers. The calculation is performed based on finite element method via the COMSOL software. Structured quadrilateral meshes can be obtained by partitioning the entire geometric domain through mapping operations. The accuracy of numerical simulation results is usually related to the mesh quality (Krzywanski et al., 2020a; Krzywanski et al., 2020b). According to the grid quality check, the quality of the mesh increases with the increasing element numbers. Here, A mesh-size and time-step independence study is carried out by analyzing the transient uptake of the adsorbent and average temperature. As listed in Table 3, a sufficiently accurate grid-independent solution was obtained with a time step of 1 s and a total mesh size of 960, where the maximum element size is 1.04×10^{-4} m and the minimum element size is 4.6×10^{-5} m.

Validation of the computational fluid dynamic model of AD is conducted via comparing the transient experimental temperature and uptake obtained by Mohammed et al. (Mohammed et al., 2018) with the numerical results based on present mathematical model. As depicted in Fig. 3, good accordance between the simulation results and the experimental data is observed. The average relative errors of the temperature and adsorbate uptake between the calculated and experimental data are 0.23 % and 2.92 %, respectively, which validates the CFD model presented in this study.

3. Results and discussion
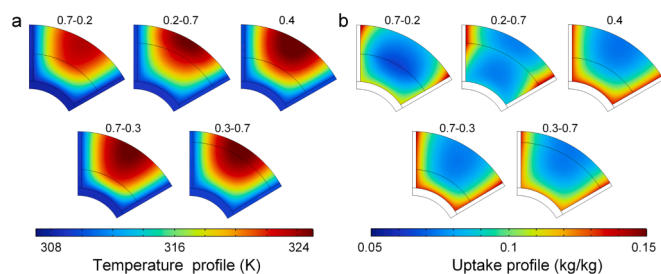
3.1. Effect of stepwise porosity distribution

The porosity distributions of the adsorbent in the adsorption bed can significantly affect the performance of the adsorption-based power and refrigeration cogeneration system. Fig. 4 presents the temperature and uptake profiles of the adsorbent bed under various stepwise porosity distributions at the adsorption time of 400 s. The effective local thermal conductivity of the adsorbent bed can be calculated as $k_b = k_\nu \varepsilon_b + k_s(1 - \varepsilon_b)$. Smaller porosity renders higher effective local thermal conductivity. Thus, Configuration I has larger local effective thermal conductivity near the surface of the heat exchange tube, while the Configuration II has larger local effective thermal conductivity near the vapor inlet zone. As seen in Fig. 4a, the temperature distribution in Configuration II is more uniform than that in Configuration I. This can be attribute to that larger effective thermal conductivity near the vapor inlet zone facilitates heat transfer in the adsorbent bed. The sorption heat generated at the inlet section can be effectively transferred to the zone near the heat exchange tube. In Configuration I, larger thermal conductivity near the metal tube promotes the heat exchange of the adsorption bed with the external hot/cold water. As the adsorption process is exothermic, a lower temperature is beneficial for the enhancement of adsorption uptake.

It can be seen from Fig. 4b that higher uptake is distributed in the region with lower temperature. Furthermore, compared with the uniform distribution, the adsorption uptake is enhanced in the SPZ due to higher effective thermal conductivity, which is weakened in the LPZ induced by lower effective thermal conductivity. As depicted in Fig. 5a, the uptake degradation in the LPZ is more pronouncing than the uptake enhancement in the SPZ. A smaller porosity in the LPZ leads to larger water production at a given porosity in the SPZ. The water production in

Table 2
Detailed initial and boundary conditions.

Initial conditions	
$P = P_{sat}@T_{eva}$; $X = X_0@(T = 60°C, P = P_{eva})$; $M_{sw} = 50$ kg	
Boundary conditions	
In the isobaric heating process	$T_f = T_{hw}$
In the desorption process	$T_f = T_{hw}$; $P(R) = P_{con}$
In the isobaric cooling process	$T_f = T_{cw}$
In the absorption process	$T_f = T_{hw}$; $P(R) = P_{eva}$

Table 3

Results of mesh-size and time-step independence study.

Time step	0.5 s						1 s					
Mesh size	960		1320		1666		960		1320		1666	
Time	W_{av}	T_{av}	W_{av}	T_{av}	W_{av}	T_{av}	W_{av}	T_{av}	W_{av}	T_{av}	W_{av}	T_{av}
100	0.0494	327.85	0.0494	327.86	0.0494	327.86	0.0494	327.85	0.0494	327.86	0.0494	327.86
250	0.0661	324.83	0.0661	324.84	0.0661	324.84	0.0661	324.83	0.0661	324.84	0.0661	324.84
400	0.0794	322.04	0.0794	322.05	0.0794	322.05	0.0794	322.04	0.0794	322.05	0.0793	322.05
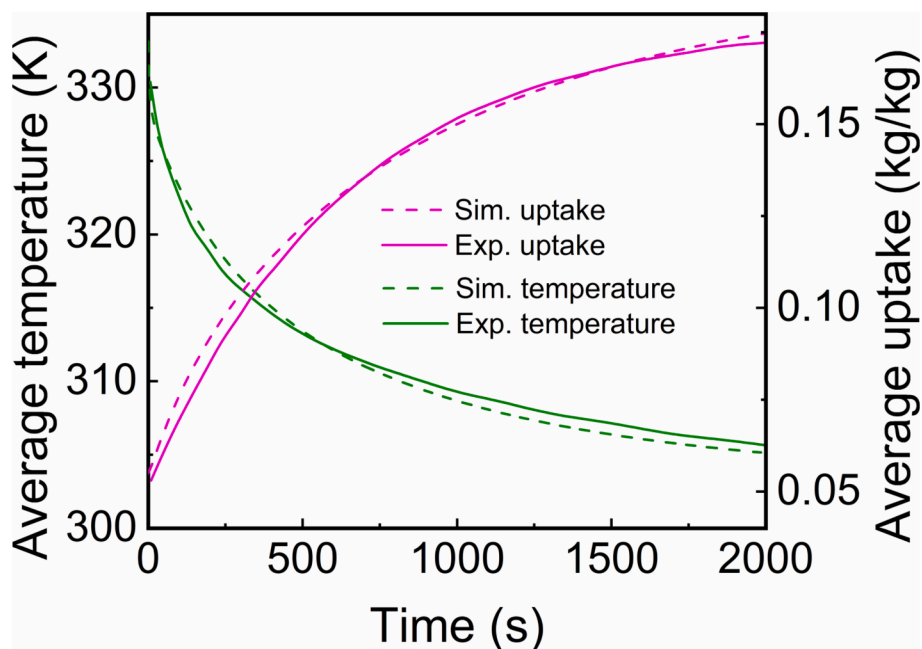
Fig. 3. Comparison of average temperature and uptake during adsorption process in present simulation and that of Mohammed et al (Mohammed et al., 2018).

Fig. 4. Temperature profiles (a) and uptake profiles (b) of the adsorbent bed under different stepwise porosity distributions at the adsorption time of 400 s.

the distributions with a porosity of 0.3 in the SPZ is greater than that with a porosity of 0.2 in the SPZ, which benefits from shrinked LPZ with lower effective thermal conductivities. The uniform distribution with an adsorbent porosity of 0.4 renders the maximum water production. As seen in Fig. 4b, for distributions with a porosity of 0.2 in the SPZ, Configuration I exhibits higher water production than Configuration II, as the uptake in the LPZ of Configuration II is significantly undermined. While for distributions with a porosity of 0.3 in the SPZ, the uptake of Configuration I in the LPZ is weakened more significantly than that of Configuration II, leading to lowered water production. The increase of water production contributes to the power generation. Hence the electric power is positively correlated with water production, as shown in Fig. 5b. The latent heat of solvent evaporation in the evaporator is used to generate cooling power and maintain the temperature variation in the evaporator. The cooling power is not directly proportional to the water

production, which is also affected by the evaporation temperature, as shown in Fig. 5c. It can be seen from Fig. 5d that the regeneration heat of Configuration I is larger than that of Configuration II, which can be attribute to the more sufficient heat exchange between the adsorption bed and external heat source. Increasing porosity in the SPZ at the same porosity in the LPZ and decreasing porosity in the LPZ at the same porosity in the SPZ both contribute to regeneration heat.

As shown in Fig. 6, the COP of the power and refrigeration cogeneration system shows the same trend as the cooling power. The electrical efficiency is significantly affected by the regeneration heat. Considering the difference in energy quality between cooling power and electric power, exergy efficiency is introduced to evaluate the overall performance of the cogeneration system. As shown in Fig. 6c the exergy efficiency exhibits the same trend with the cooling power, as the magnitude of cooling power is much larger than that of the electricity. Compared with the uniform porosity configuration of 0.4, the COP and exergy efficiency are respectively elevated by 1.96 % and 1.19 % under the stepwise porosity distribution of 0.3–0.5; The electrical efficiency is elevated by 15.5 % under the stepwise porosity configuration of 0.7–0.2. Configuration I is benefit for COP and exergy efficiency, which Configuration II contributes to the electrical efficiency. In both configurations, increasing porosity in SPZ and decreasing porosity in LPZ lead to higher COP, higher exergy efficiency and lower electrical efficiency.

3.2. Effect of adsorption time

Adsorption/desorption time refers to the period when the adsorption bed is connected with evaporator/condenser for adsorption/desorption, while producing concentrated/diluted solution. Fig. 7 represents the
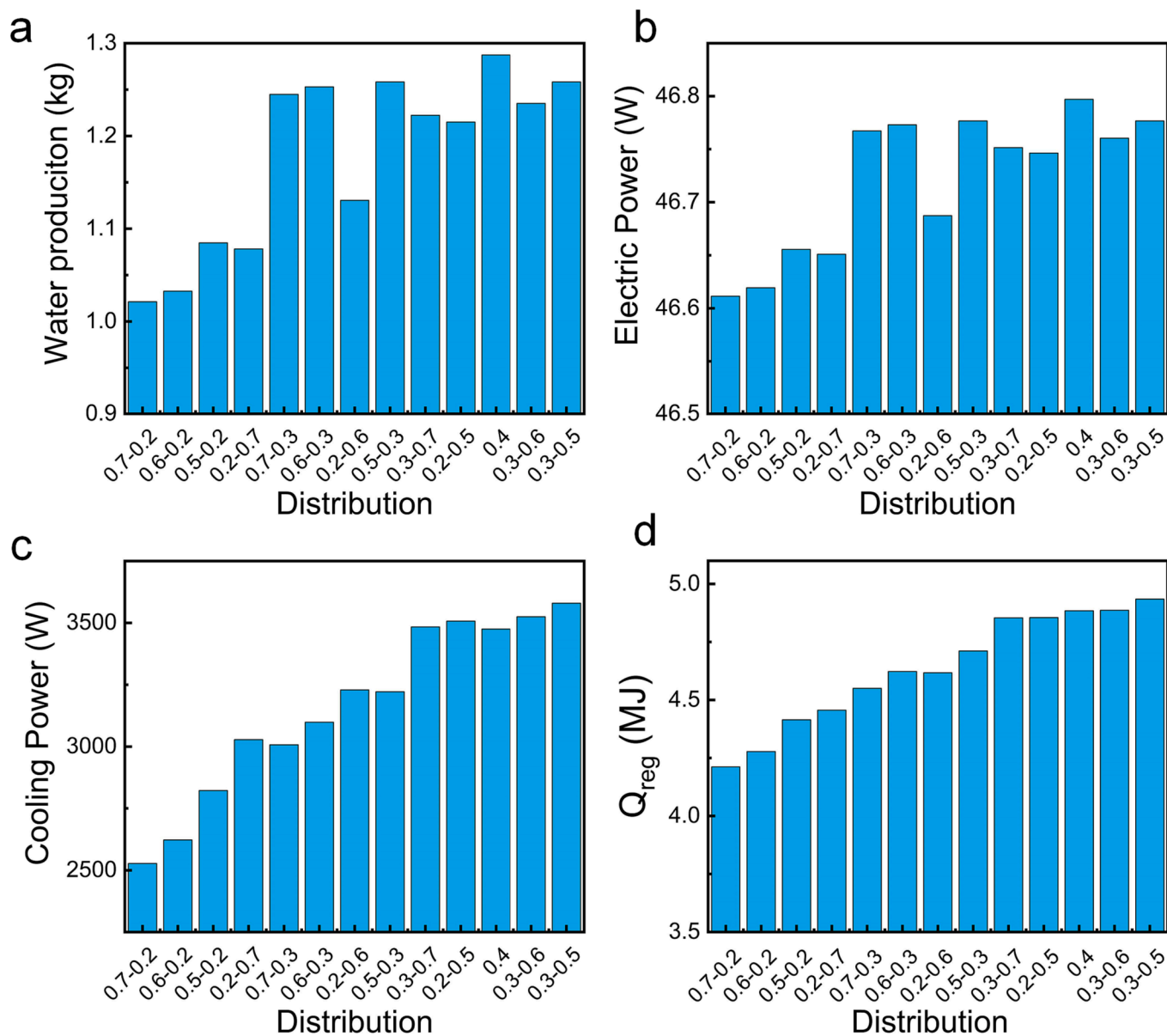
Fig. 5. Water production (a), electric power (b), cooling power (c) and regeneration heat (d) under various stepwise porosity distributions.
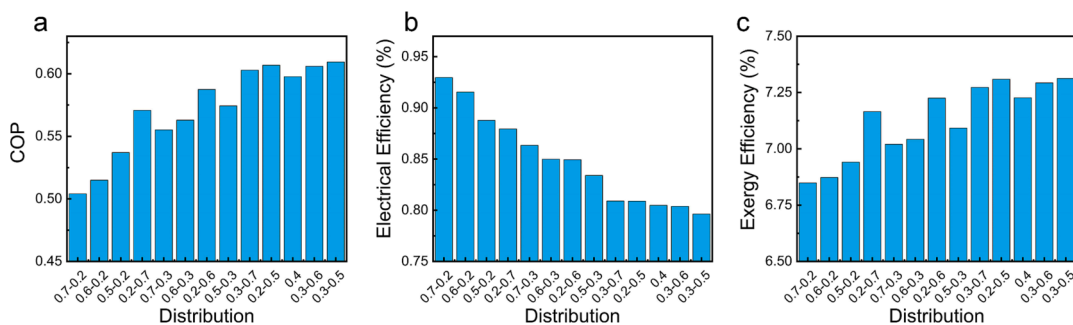

Fig. 6. Coefficient of performance (a), electrical efficiency (b) and exergy efficiency (c) under various stepwise porosity distributions.

temperature profiles of the adsorbent bed at the end of different adsorption time under the stepwise porosity distribution of 0.2–0.7. The adsorbent bed is cooled more sufficiently at a longer adsorption time, which contributes to the water production, thus the electricity extracted and cooling capacity, as shown in Fig. 8. Although larger adsorption

time leads to higher electricity extracted, it extends the cycle period, resulting in the reduced electric power (Fig. 8b). Under a shorter adsorption time, the increase of cooling capacity is more obvious than the increase of cycle period, resulting in increased cooling power, while the increasing cycle period acts dominantly under a longer adsorption
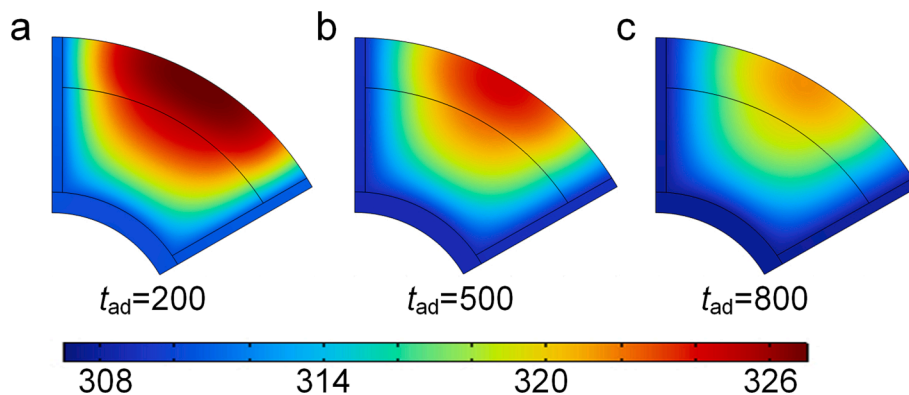
Fig. 7. Temperature profiles of the adsorbent bed at the end of different adsorption time under the stepwise porosity distribution of 0.2–0.7.
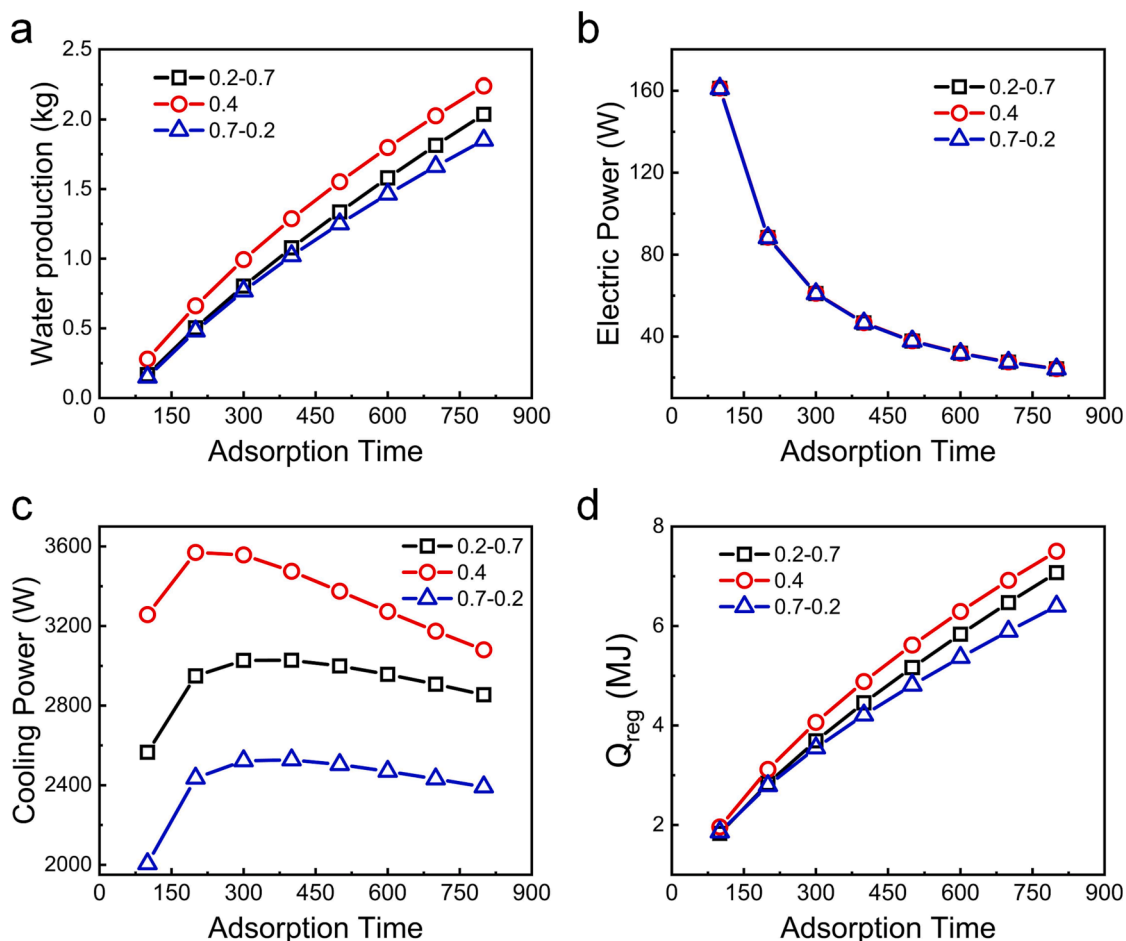

Fig. 8. Water production (a), electric power (b), cooling power (c) and regeneration heat (d) under various adsorption time for different stepwise configurations.

time, leading to decreased cooling power, as depicted in Fig. 8c. Therefore, the cooling power first increases with increasing adsorption/desorption time, reaches its maximum value, then decreases. Large adsorption/desorption time contributes to desorption process. And more regeneration heat is required for preheating the adsorption bed and desorbing the water vapor to maintain the thermodynamic cycle (Fig. 8d).

Fig. 9 shows the variation of the COP, electrical efficiency and exergy efficiency under different adsorption time for different stepwise porosity configurations. Despite augmented regeneration heat at larger adsorption time, the impact of the elevated cooling capacity is more significantly, leading to increased COP at larger adsorption time. The electrical

efficiency and exergy efficiency decrease with the increasing adsorption time due to the significantly enlarged regeneration heat. The stepwise porosity distribution of 0.7–0.2 renders the highest electric efficiency owning to the lowest heat consumption, while it leads to the lowest exergy efficiency due to the lowest cooling capacity. Compared to the uniform porosity, the electrical efficiency can be improved by 16.67 % under the stepwise porosity distribution of 0.7–0.2 at the adsorption time of 800 s.

3.3. Effect of switching time

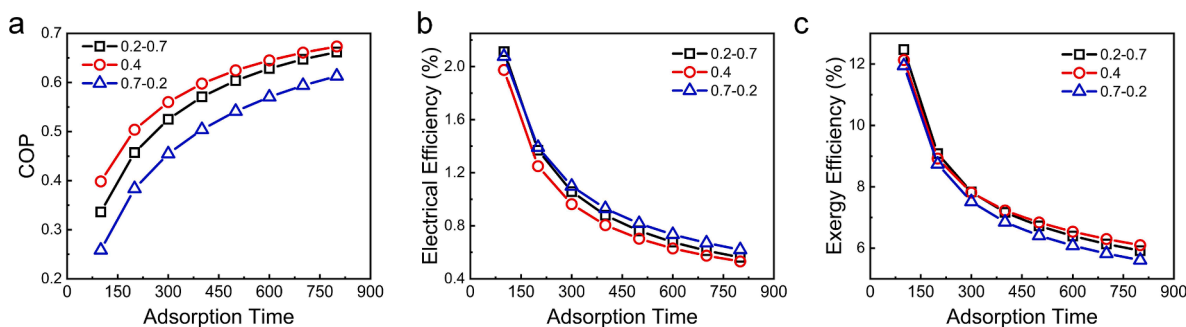During the switching process before adsorption/desorption, the

Fig. 9. Coefficient of performance (a), electrical efficiency (b) and exergy efficiency (c) under various adsorption time for different stepwise porosity configurations.

adsorption bed is precooled/preheated to reduce/elevate the temperature and pressure for matching up the pressure in the evaporator/condenser. Fig. 10 depicts the temperature profiles of the adsorbent bed at the end of the switching process before adsorption under the stepwise porosity distribution of 0.2–0.7. The adsorption bed can be cooled more sufficiently at a larger switching time, which lead to a higher maximum uptake.

Larger switching time can improve bed temperature before desorption process, thereby elevating the pressure in the bed chamber, which leads to unexpected desorption. At the beginning of desorption process, the desorped vapor condensed in the condenser results in undesirable elevated condensation pressure, which undermines the desorption process and increases the minimum adsorption capacity. The working capacity of the adsorbent can be calculated by the difference between maximum uptake and minimum uptake. Therefore, neither too long nor too short switching time is applicable. An appropriate switching time is anticipated. As seen in Fig. 11a, under stepwise porosity configurations of 0.2–0.7 and 0.7–0.2, the water production increases with increasing switching time due to higher maximum uptake induced by better-precooled adsorption bed. Under the uniform porosity configuration of 0.4, the water production increases at shorter switching time. The effect of the increase of minimum uptake due to the elevated desorption pressure is more significant at longer switching time. There exits an optimal switching time leading to the largest water production. Although the electricity extracted and cooling capacity is proportional to the water production, the electric power and cooling power decrease with increasing switching time due to significantly augmented cycle time.

The COP, electrical efficiency and exergy efficiency under various switching time are depicted in Fig. 12. The COP under stepwise porosity configurations of 0.2–0.7 and 0.7–0.2 increase monotonously with the increase of switching time. While the COP under uniform porosity configuration increases first, reaches the maximum value, and then decreases, which are consistent with the trend of cooling capacity
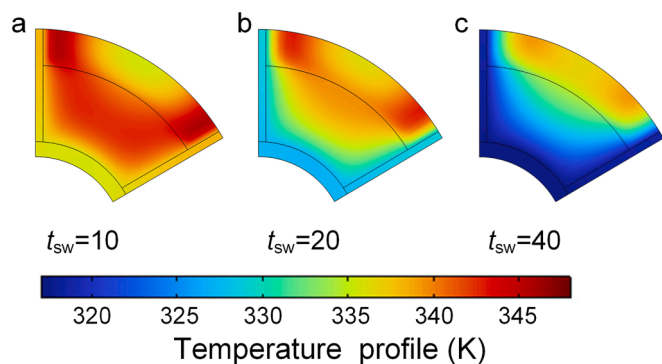
(Fig. 11a). The exergy efficiency under the stepwise porosity distributions of 0.2–0.7 and 0.7–0.2 decreases with the increase of switching time due to significantly elevated regeneration heat. Under the uniform porosity configuration of 0.4, the exergy efficiency decreases due to the increasing regeneration heat at shorter switching time; At longer switching time, the reduction of both cooling capacity and power generation hinder the exergy efficiency. Compared with the electrical efficiency under the uniform porosity configuration, the electrical efficiency can be improved by 16.21 % under the stepwise porosity distribution of 0.7–0.2 at the switching time of 10 s. Configuration I renders higher COP and exergy efficiency while Configuration II exhibits upgraded electrical efficiency.

3.4. Effect of fin number

Fins attached on the heat exchanger tube augments the heat exchange area, which facilitates the removal/supply of the adsorption/regeneration heat, thus benefitting the adsorption/desorption process. Fig. 13 shows the temperature profiles of the adsorbent bed under the stepwise porosity configuration of 0.2–0.7 for different fin numbers at the end of the adsorption process. It can be seen that larger fin number leads to low average temperature of the adsorption bed due to better heat transfer characteristics.

As shown in Fig. 14a, the water production increases with increasing fin numbers for all the studied porosity distributions. The electric power and cooling power present the same tendency as water production, originating from the fact that larger water production results in larger Gibbs free energy of mixing and more latent heat taken away from evaporator. The heat transfer from hot water to the mental tube in improved at larger fin numbers due to the increasing heat exchange area.

Fig. 15 depicts the overall performance of the cogeneration system. The COP under the stepwise porosity configuration of 0.2–0.7 decreases with increasing fin numbers as the increase of heat consumption overrides that of cooling capacity. While the enhanced cooling capacity is more significant under the stepwise porosity configuration of 0.7–0.2, resulting in enhanced COP. The performance under the uniform porosity configuration of 0.4 is less sensitive to fin numbers, as the effects of the both elevated heat consumption and cooling capacity compensate for each other. The electrical efficiency and exergy efficiency decrease with increasing fin numbers due to significantly elevated regeneration heat. Compared to Configuration I, Configuration II of 0.7–0.2 renders lower COP and exergy efficiency as well as higher electrical efficiency due to much lower regeneration heat. Compared to the uniform porosity configuration, the electrical efficiency can be improved by 16.21 % under the stepwise porosity distribution of 0.7–0.2, and the exergy efficiency can be improved by 1.09 % under the stepwise porosity distribution of 0.2–0.7 at the fin number of 4.
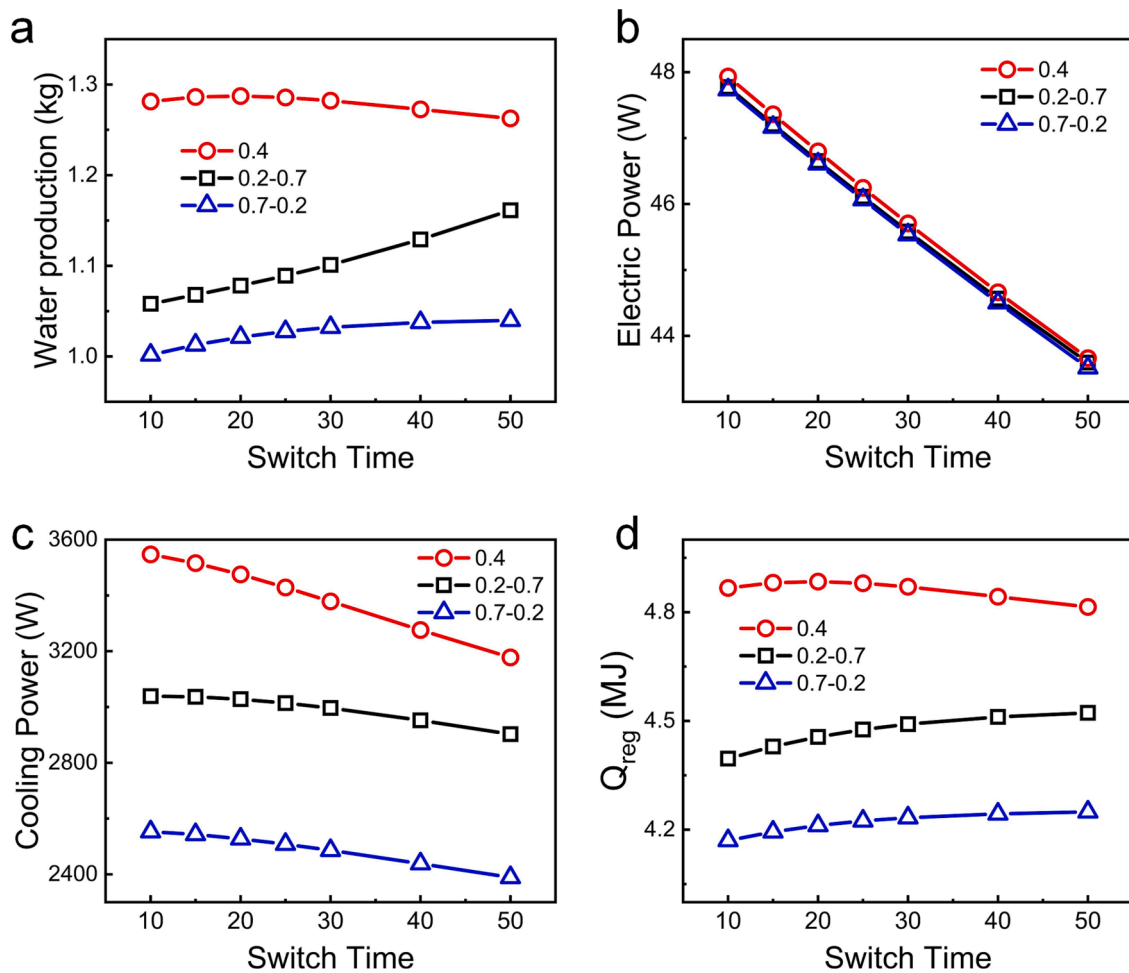

Fig. 10. Temperature profiles of the adsorbent bed under the end of different switching time before adsorption at a stepwise porosity distribution of 0.2–0.7.

Fig. 11. Water production (a), electric power (b), cooling power (c) and regeneration heat (d) under various switching time for different stepwise configurations.
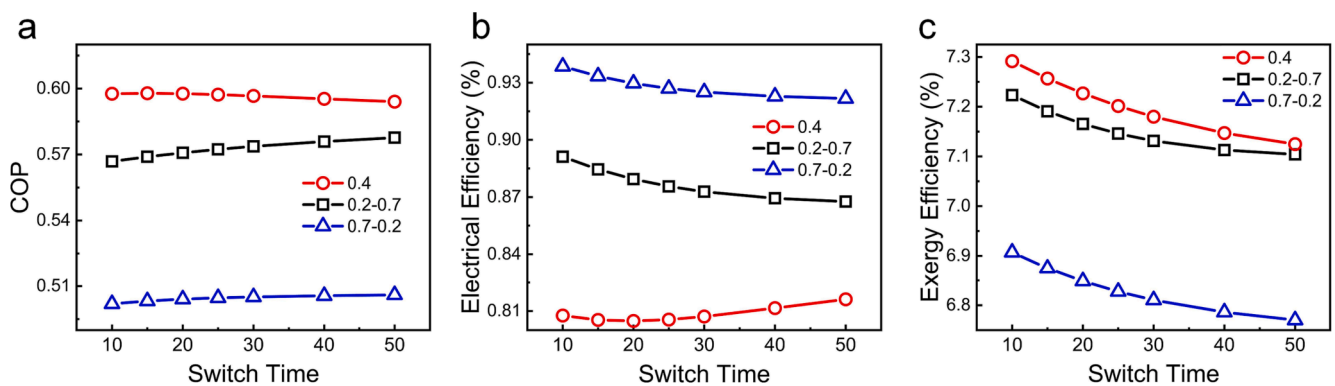

Fig. 12. Coefficient of performance (a), electrical efficiency (b) and exergy efficiency (c) under various switching time for different stepwise configurations.

3.5. Effect of working solution-adsorbent pairs

Working adsorbent with different physical properties and adsorption isotherms can significantly impact the heat and mass transfer in the adsorption bed. In the evaporator, working salts with different osmotic coefficients can significantly impact the evaporation pressure, thus the adsorption process and refrigeration performance. In addition, working salts with different activity coefficients can also affect the power extracted. Here, five kinds of salts (LiCl, LiNO$_3$, NaCl, NaNO$_3$, and AgNO$_3$) are employed for preparing the working solution; Two common adsorbents of AQSOA-Z02 and Silica gel are applied. As shown in

Fig. 16, among the studied five salts, LiCl renders the highest electrical efficiency while it leads to the lowest COP; AgNO$_3$ renders the highest COP while it results in lowest electrical efficiency. Compared with AQSOA-Z02, silica gel leads to higher COP. However, it renders lower electrical efficiency. For all the stepwise porosity distributions, Configuration II results in higher electrical efficiency and lower COP than Configuration I. Compared with uniform porosity of 0.4, the electrical efficiency is elevated and the COP is degraded under both configurations. With AQSOA-Z02 as the adsorbent, the exergy efficiency of Configuration II is higher than that of Configuration I due to the higher electricity extracted. With Silica gel as the adsorbent, the exergy
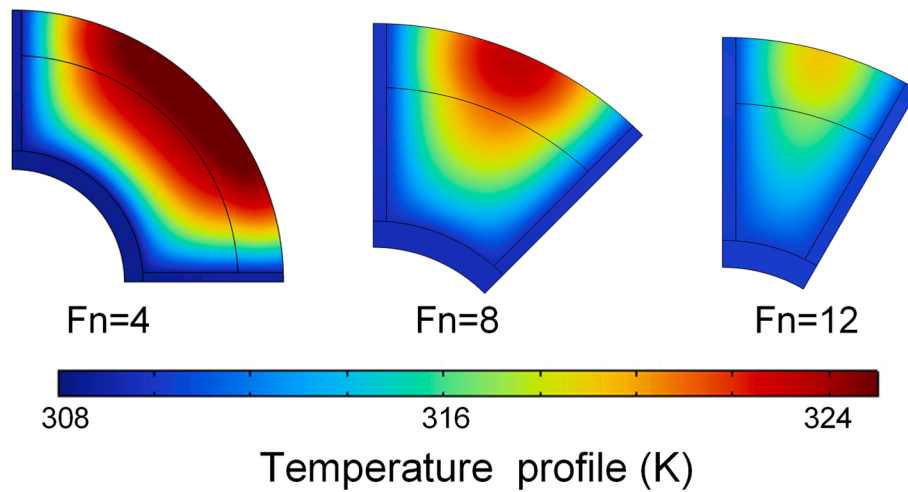
Fig. 13. Temperature profiles of the adsorbent bed with the stepwise porosity configuration of 0.2–0.7 under different fin numbers at the end of the adsorption process.
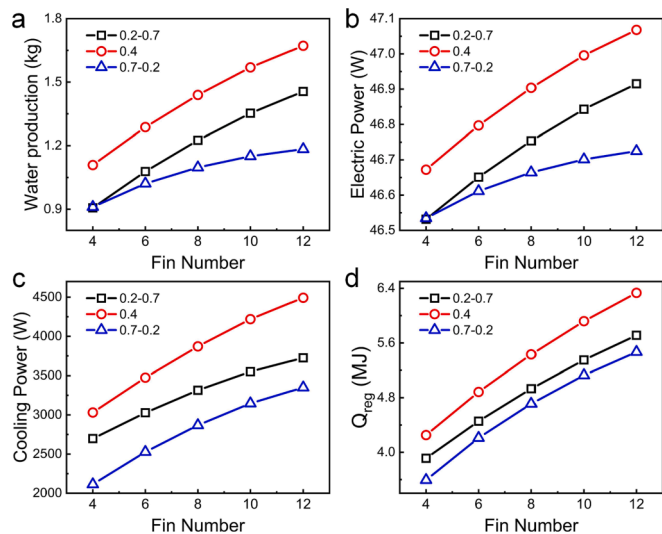

Fig. 14. Water production (a), electric power (b), cooling power (c) and regeneration heat (d) under various fin number for different stepwise porosity configurations.

efficiency of Configuration I is higher than that of Configuration II due to the larger cooling capacity. The working pairs of LiCl and AQSOA-Z02 under the stepwise porosity configuration of 0.7–0.2 leads to the highest exergy efficiency and electrical efficiency of 7.76 % and 1.32 %. The

working pairs of AgNO$_3$ and Silica gel under the uniform porosity configuration leads to the highest COP of 0.57. For comparison, the electrical efficiency of the adsorption-based OHE obtained via solving lumped model are collected from previous literatures in Table 4, where the porosity of the adsorbent is always assumed to be uniform.

4. Conclusions

In this study, an adsorption-based osmotic heat engine combining AD with RED for converting the low-grade heat into electricity as well as providing refrigeration is presented. Considering the heat and mass transfer characteristics in the adsorption bed, a two-dimensional computational fluid dynamic model of a finned-tube adsorption bed with stepwise porosity distributions is proposed. The effects of the stepwise porosity distribution, adsorption time, switching time, fin number and working pairs on system performance are comprehensively analyzed under different stepwise distribution configurations. The main findings are listed below:

(1) Configuration I leads to higher COP and exergy efficiency while Configuration II presents a larger electrical efficiency. In both configurations, increasing porosity in SPZ at a given porosity in the LPZ and decreasing porosity in LPZ at a given porosity in the SPZ lead to higher COP, higher exergy efficiency and lower electrical efficiency. Compared with the uniform porosity configuration of 0.4, COP and exergy efficiency are respectively elevated by 1.96 % and 1.19 % under the stepwise porosity
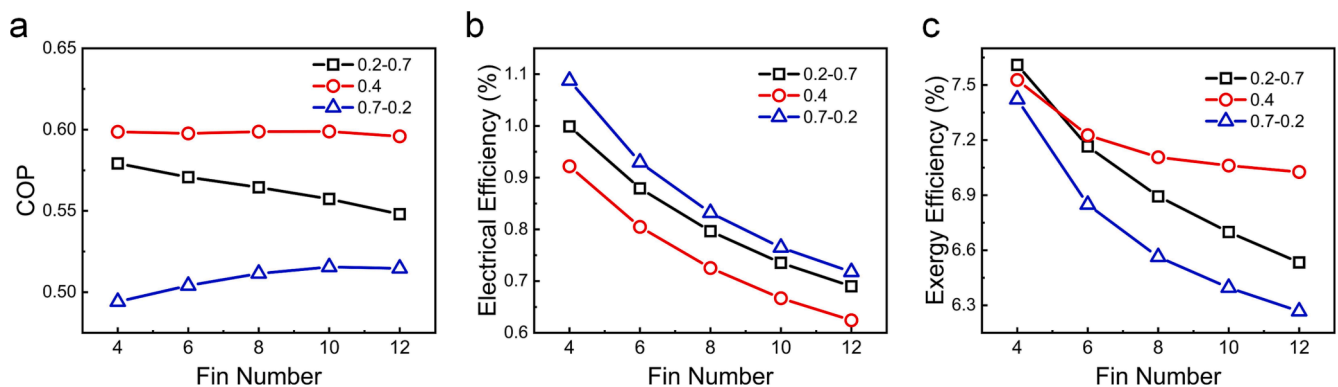

Fig. 15. Coefficient of performance (a), electrical efficiency (b) and exergy efficiency (c) under various fin number for different stepwise porosity configurations.
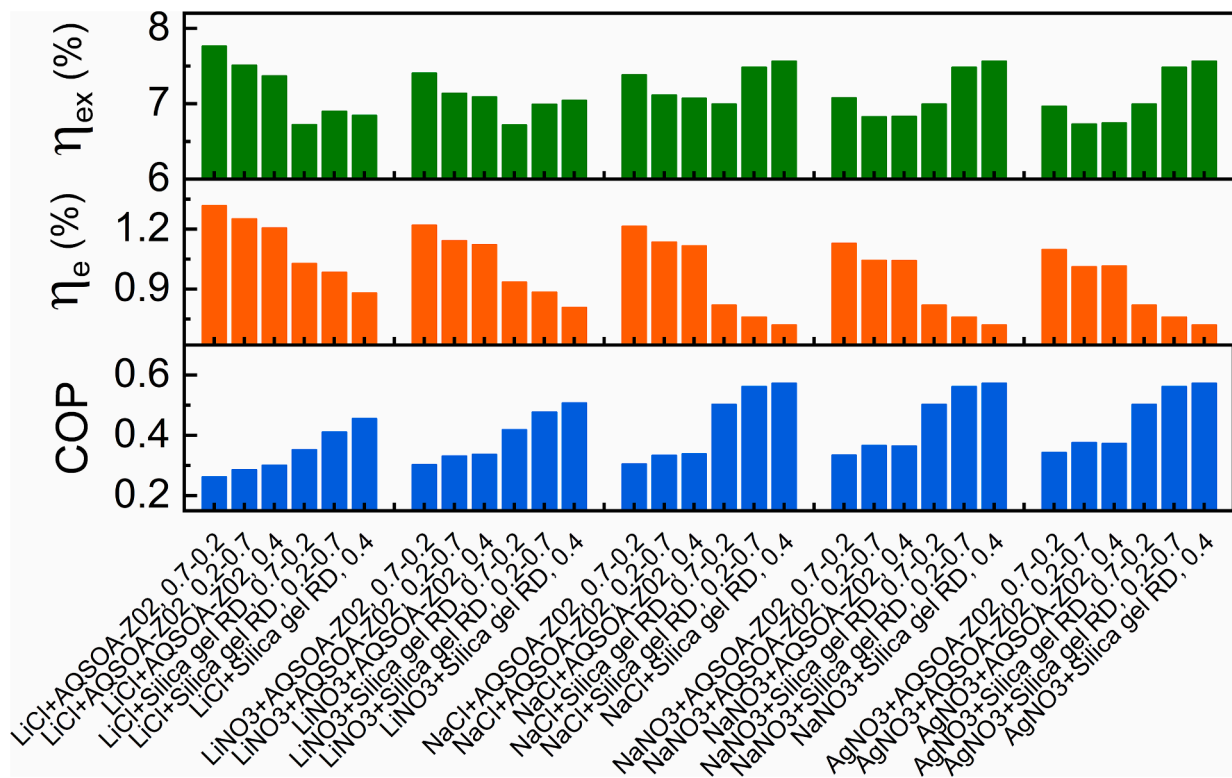
Fig. 16. Coefficient of performance, electrical efficiency and exergy efficiency under various working pairs for different configurations.

Table 4
Electrical efficiency of the adsorption-based OHE in previous literatures.

Architecture	Working solution	Working concentration	Energy/Electrical efficiency	Ref.
AD-RED	LiCl-water	20 mol/kg	4 %	(Olkis et al., 2018)
AD-RED	NaCl-water	5 mol/L	0.55 %	(Olkis et al., 2020)
AD-RED	NaCl-water	8 mol/kg	0.39 %	(Zhao et al., 2020)
AD-RED	NaCl-water	7 mol/kg	1.08 %	(Zhao et al., 2021)
AD-RED	NaCl-water	7 mol/kg	1.04 %	(Zhao et al., 2021)

configuration of 0.3–0.5. The electrical efficiency is increased by 15.5 % with porosity configuration of 0.7–0.2.

(2) Longer adsorption and switching time results in higher COP. However, they hinder the electrical efficiency and exergy efficiency under the stepwise porosity distributions. With the increase of fin number, COP increases under the stepwise porosity distribution of 0.7–0.2, while it decreases under the stepwise porosity distribution of 0.2–0.7. For uniform porosity distribution, COP is less sensitive to increasing fin number and remains almost invariant. Larger fin number results in lower electrical efficiency and exergy efficiency.

(3) The trade-off between refrigeration and electricity generation can be clearly observed under different salt solution-adsorbent working pairs. LiCl renders the highest electrical efficiency while it leads to the lowest COP; AgNO3 renders the highest COP

while it results in lowest electrical efficiency. Compared with AQSOA-Z02, silica gel leads to higher COP. However, it renders lower electrical efficiency. With AQSOA-Z02 as the adsorbent, the exergy efficiency of Configuration II is higher than that of Configuration I due to the higher electricity extracted. With Silica gel as the adsorbent, the exergy efficiency of Configuration I is higher than that of Configuration II due to the larger cooling capacity.

Declaration of Competing Interest

The authors declare that they have no known competing financial interests or personal relationships that could have appeared to influence the work reported in this paper.

Data availability

Data will be made available on request.

References

Askalany, A.A., Salem, M., Ismail, I.M., Ali, A.H.H., Morsy, M.G., 2012. Experimental study on adsorption–desorption characteristics of granular activated carbon/R134a pair. Int. J. Refrig 35 (3), 494–498.

Aziz, M.A., Gad, I.A.M., Mohammed, E.S.F.A., Mohammed, R.H., 2012. Experimental and numerical study of influence of air ceiling diffusers on room air flow characteristics. Energ. Buildings 55, 738–746.

Bird, R.B., 2002. Transport phenomena. Appl. Mech. Rev. 55 (1), R1–R4.

Brogioli, D., Yip, N.Y., 2022. Energy efficiency analysis of membrane distillation for thermally regenerative salinity gradient power technologies. Desalination 531, 115694.

Brough, D., Jouhara, H., 2020. The aluminium industry: A review on state-of-the-art technologies, environmental impacts and possibilities for waste heat recovery. Int. J. Thermofluids 1–2, 100007.

Cai, S., Hua, Z., Dai, M., Li, S., Luo, X., Tu, Z., 2023. Investigation of stepwise porosity and perforated fins in finned tube adsorption bed for adsorption refrigeration. Appl. Therm. Eng. 229, 120587.

Chen, W.D., Chua, K.J., 2020. Parameter analysis and energy optimization of a four-bed, two-evaporator adsorption system. Appl. Energy 265.

Demir, H., Mobedi, M., Ülkü, S., 2009. Effects of porosity on heat and mass transfer in a granular adsorbent bed. Int. Commun. Heat Mass Transfer 36 (4), 372–377.

Egilegor, B., Jouhara, H., Zuazua, J., Al-Mansour, F., Plesnik, M., Montorsi, L., et al., 2020. ETEKINA: Analysis of the potential for waste heat recovery in three sectors: Aluminium low pressure die casting, steel sector and ceramic tiles manufacturing sector. Int. J. Thermofluids. 1–2, 100002.

Grabowska, K., Sztekler, K., Krzywanski, J., Sosnowski, M., Stefanski, S., Nowak, W., 2021. Construction of an innovative adsorbent bed configuration in the adsorption chiller part 2. experimental research of coated bed samples. Energy 215, 119123.

Hua, W.S., Xu, H.J., Xie, W.H., 2022. Review on adsorption materials and system configurations of the adsorption desalination applications. Appl. Therm. Eng. 204, 117958.

Kim, B., Seo, J.Y., Chung, C.-H., 2020. A hybrid system of capacitive deionization and redox flow battery for continuous desalination and energy storage. J. Power Sources 448, 227384.

Krzywanski J, Sztekler K, Szubel M, Siwek T, Nowak W, Mika Ł. A Comprehensive, Three-Dimensional Analysis of a Large-Scale, Multi-Fuel, CFB Boiler Burning Coal and Syngas. Part 2. Numerical Simulations of Coal and Syngas Co-Combustion. Entropy2020.

Krzywanski J, Sztekler K, Szubel M, Siwek T, Nowak W, Mika Ł. A Comprehensive Three-Dimensional Analysis of a Large-Scale Multi-Fuel CFB Boiler Burning Coal and Syngas. Part 1. The CFD Model of a Large-Scale Multi-Fuel CFB Combustion. Entropy2020.

Krzywanski, J., Grabowska, K., Sosnowski, M., Zylka, A., Kulakowska, A., Czakiert, T., et al., 2022. Heat Transfer in Adsorption Chillers with Fluidized Beds of Silica Gel, Zeolite, and Carbon Nanotubes. Heat Transfer Eng. 43 (3–5), 172–182.

Krzywanski, J., Skrobek, D., Zylka, A., Grabowska, K., Kulakowska, A., Sosnowski, M., et al., 2023. Heat and mass transfer prediction in fluidized beds of cooling and desalination systems by AI approach. Appl. Therm. Eng. 225, 120200.

Kulakowska, A., Pajdak, A., Krzywanski, J., Grabowska, K., Zylka, A., Sosnowski, M., et al., 2020. Effect of Metal and Carbon Nanotube Additives on the Thermal Diffusivity of a Silica Gel-Based Adsorption Bed. Energies.

Leong, K.C., Liu, Y., 2004. Numerical modeling of combined heat and mass transfer in the adsorbent bed of a zeolite/water cooling system. Appl. Therm. Eng. 24 (16), 2359–2374.

Li, M., Zhao, Y., Long, R., Liu, Z., Liu, W., 2021. Gradient porosity distribution of adsorbent bed for efficient adsorption cooling. Int. J. Refrig 128, 153–162.

Li, M., Zhao, Y., Long, R., Liu, Z., Liu, W., 2022. Metal foam packed adsorbent bed boosting the performance of the adsorption-based desalination and cooling system. Energ. Conver. Manage. 254, 115250.

Liu, Z., Lu, D., Dong, Y., Bai, Y., Shen, T., Chen, H., et al., 2022. Performance improvement of LiBr-H2O reverse electrodialysis unit for heat to power conversion with finite solution flowrate and large concentration change. Energ. Conver. Manage. 270, 116263.

Liu, Z., Lu, D., Bai, Y., Zhang, J., Gong, M., 2022. Energy and exergy analysis of heat to salinity gradient power conversion in reverse electrodialysis heat engine. Energ. Conver. Manage. 252, 115068.

Long, R., Li, B., Liu, Z., Liu, W., 2017. Hybrid membrane distillation-reverse electrodialysis electricity generation system to harvest low-grade thermal energy. J. Membr. Sci. 525, 107–115.

Long, R., Xia, X., Zhao, Y., Li, S., Liu, Z., Liu, W., 2021. Screening metal-organic frameworks for adsorption-driven osmotic heat engines via grand canonical Monte Carlo simulations and machine learning. iScience. 24 (1), 101914.

Marino, M., Misuri, L., Ruffo, R., Brogioli, D., 2015. Electrode kinetics in the "capacitive mixing" and "battery mixing" techniques for energy production from salinity differences. Electrochim. Acta 176, 1065–1073.

Mohammed, R.H., 2013. A simplified method for modeling of round and square ceiling diffusers. Energ. Buildings 64, 473–482.

Mohammed, R.H., Mesalhy, O., Elsayed, M.L., Chow, L.C., 2018. Scaling analysis of heat and mass transfer processes in an adsorption packed bed. Int. J. Therm. Sci. 133, 82–89.

Olkis, C., Santori, G., Brandani, S., 2018. An Adsorption Reverse Electrodialysis system for the generation of electricity from low-grade heat. Appl. Energy 231, 222–234.

Olkis, C., Brandani, S., Santori, G., 2019. A small-scale adsorption desalinator. Energy Procedia 158, 1425–1430.

Olkis, C., Brandani, S., Santori, G., 2020. Adsorption reverse electrodialysis driven by power plant waste heat to generate electricity and provide cooling. Int. J. Energy Res.

Olkis, C., Brandani, S., Santori, G., 2021. Adsorption reverse electrodialysis driven by power plant waste heat to generate electricity and provide cooling. Int. J. Energy Res. 45 (2), 1971–1987.

Oyekale, J., Emagbetere, E., 2022. A review of conventional and exergetic life cycle assessments of organic Rankine cycle plants exploiting various low-temperature energy resources. Heliyon. 8 (7), e09833.

Pitzer, K.S., Mayorga, G., 1973. Thermodynamics of electrolytes. II. Activity and osmotic coefficients for strong electrolytes with one or both ions univalent. J. Phys. Chem. 77 (19), 2300–2308.

Prajapati, M., Shah, M., Soni, B., 2022. A comprehensive review of the geothermal integrated multi-effect distillation (MED) desalination and its advancements. Groundw. Sustain. Dev. 19, 100808.

Rahman, A., Farrok, O., Haque, M.M., 2022. Environmental impact of renewable energy source based electrical power plants: Solar, wind, hydroelectric, biomass, geothermal, tidal, ocean, and osmotic. Renew. Sustain. Energy Rev. 161, 112279.

Raninga, M., Mudgal, A., Patel, V.K., Patel, J., 2022. Design of ORC-RO system for utilizing waste heat from flue gases of coal-fired thermal power plant. Mater. Today:. Proc.

Silvester, L.F., Pitzer, K.S., 1977. Thermodynamics of electrolytes. 8. High-temperature properties, including enthalpy and heat capacity, with application to sodium chloride. J. Phys. Chem. 81 (19), 1822–1828.

Solmuş, İ., Andrew, S., Rees, D., Yamalı, C., Baker, D., 2012. A two-energy equation model for dynamic heat and mass transfer in an adsorbent bed using silica gel/water pair. Int. J. Heat Mass Transf. 55 (19–20), 5275–5288.

Sztekler, K., Kalawa, W., Nowak, W., Mika, Ł., Krzywański, J., Grabowska, K., et al., 2020. Performance Evaluation of a Single-Stage Two-Bed Adsorption Chiller With Desalination Function. J. Energy Res. Technol. 143 (8).

Sztekler, K., Kalawa, W., Nowak, W., Mika, L., Gradziel, S., Krzywanski, J., et al., 2020. Experimental Study of Three-Bed Adsorption Chiller with Desalination Function. Energies.

Tamburini, A., Cipollina, A., Papapetrou, M., Piacentino, A., Micale, G., 2016. 7 - Salinity gradient engines. In: Cipollina, A., Micale, G. (Eds.), Sustainable Energy from Salinity Gradients. Woodhead Publishing, pp. 219–256.

Taqvi, S.M., Vishnoi, A., Levan, M.D., 1997. Effect of macropore convection on mass transfer in a bidisperse adsorbent particle. Adsorption 3 (2), 127–136.

Wang, Z., Li, J., Zhang, C., Wang, H., Kong, X., 2022. Power production from seawater and discharge brine of thermal desalination units by reverse electrodialysis. Appl. Energy 314, 118977.

Wu, J.W., Biggs, M.J., Hu, E.J., 2014. Dynamic model for the optimisation of adsorption-based desalination processes. Appl. Therm. Eng. 66 (1), 464–473.

Xia, L., Liu, R., Zeng, Y., Zhou, P., Liu, J., Cao, X., et al., 2019. A review of low-temperature heat recovery technologies for industry processes. Chin. J. Chem. Eng. 27 (10), 2227–2237.

Xie, S., Qin, P., Zhang, M., Xu, J., Ouyang, T., 2022. A high-efficiency and eco-friendly design for coal-fired power plants: Combined waste heat recovery and electron beam irradiation. Energy 258, 124884.

Xu, Z.Y., Wang, R.Z., Yang, C., 2019. Perspectives for low-temperature waste heat recovery. Energy 176, 1037–1043.

Yap, K.Y., Chin, H.H., Klemeš, J.J., 2022. Solar Energy-Powered Battery Electric Vehicle charging stations: Current development and future prospect review. Renew. Sustain. Energy Rev. 169, 112862.

Yip, N.Y., Elimelech, M., 2012. Thermodynamic and Energy Efficiency Analysis of Power Generation from Natural Salinity Gradients by Pressure Retarded Osmosis. Environ. Sci. Tech. 46 (9), 5230–5239.

Zhang, H., Hao, R., Liu, X., Zhang, N., Guo, W., Zhang, Z., et al., 2022. Thermodynamic performance analysis of an improved coal-fired power generation system coupled with geothermal energy based on organic Rankine cycle. Renew. Energy 201, 273–290.

Zhang, Y., Palamara, D., Palomba, V., Calabrese, L., Frazzica, A., 2023. Performance analysis of a lab-scale adsorption desalination system using silica gel/LiCl composite. Desalination 548, 116278.

Zhang, H., Wang, H., Zhu, X., Qiu, Y.-J., Li, K., Chen, R., et al., 2013. A review of waste heat recovery technologies towards molten slag in steel industry. Appl. Energy 112, 956–966.

Zhao, Y.-j., Duan, Y.-y., Liu, Q., Cui, Y., Mohamed, U., Zhang, Y.-k., et al., 2021. Life cycle economy-environmental evaluation of coal-based CLC power plant vs. IGCC, USC and oxy-combustion power plants with/without CO2 capture. Journal of Environmental. Chem. Eng. 9 (5), 106121.

Zhao, Y., Luo, Z., Long, R., Liu, Z., Liu, W., 2020. Performance evaluations of an adsorption-based power and cooling cogeneration system under different operative conditions and working fluids. Energy 204, 117993.

Zhao, Y., Li, M., Long, R., Liu, Z., Liu, W., 2020. Dynamic modelling and analysis of an adsorption-based power and cooling cogeneration system. Energ. Conver. Manage. 222, 113229.

Zhao, Y., Li, M., Long, R., Liu, Z., Liu, W., 2021. Advanced adsorption-based osmotic heat engines with heat recovery for low grade heat recovery. Energy Rep. 7, 5977–5987.

Zhao, Y., Li, M., Long, R., Liu, Z., Liu, W., 2021. Dynamic modeling and analysis of an advanced adsorption-based osmotic heat engines to harvest solar energy. Renew. Energy 175, 638–649.

Zhao, Y., Li, M., Long, R., Liu, Z., Liu, W., 2022. Review of osmotic heat engines for low-grade heat harvesting. Desalination 527, 115571.

Zhao, Y., Liu, Z., Li, M., Long, R., Li, S., Liu, Z., et al., 2022. Screening adsorbent-working solution pairs for adsorption-driven osmotic heat engines based on experimental water adsorption isotherm database and machine learning. Process Saf. Environ. Prot. 168, 22–31.